Communications Materials

https://doi.org/10.1038/s43246-026-01212-y

Article in Press

Glaze-enabled self-healing ceramic coatings for extreme environments

Received: 9 January 2026

Accepted: 22 May 2026

Cite this article as: Mayer, A.R., Zouina, O., Chandross, M. *et al.* Glaze-enabled self-healing ceramic coatings for extreme environments. *Commun Mater* (2026). https://doi.org/10.1038/s43246-026-01212-y

Andre R. Mayer, Omar Zouina, Michael Chandross, Martin Dienwiebel, Christian Moreau & Pantcho P. Stoyanov

Glaze-Enabled Self-Healing Ceramic Coatings for Extreme Environments

Andre R. Mayer*[1], Omar Zouina[2], Michael Chandross[3], Martin Dienwiebel[2,4], Christian Moreau[1], Pantcho P. Stoyanov*[5]

[1]Department of Mechanical, Industrial & Aerospace Engineering, Concordia University, Montreal, Quebec, Canada

[2]Karlsruhe Institute of Technology KIT, Institute for Applied Materials, MicroTribology Center μTC, Strasse Am Forum, Karlsruhe, Germany

[3]Material, Physical, and Chemical Sciences Center, Sandia National Laboratories, NM, USA

[4]Fraunhofer-Institute for Mechanics of Materials IWM, MicroTribology Center μTC, Woehlerstrasse, Freiburg, Germany

[5]Department of Chemical and Materials Engineering, Concordia University, Montreal, Quebec, Canada

Correspondence: andre.mayer@concordia.ca / pantcho.stoyanov@concordia.ca

Gas turbine engines operate under extreme thermal and mechanical stresses, where material degradation through crack formation and surface wear remains a critical challenge. Here, we report a self-healing coating system based on phase segregation in the $CoO–Cr_2O_3$ system that autonomously repairs thermally induced cracks at elevated temperatures. Mimicking the naturally formed glaze layers found in cobalt-based superalloys, these coatings not only enhance lubricity through the in-situ formation of cobalt oxides but also exhibit intrinsic damage tolerance. Crack healing occurs via defect-driven diffusion and segregation of cobalt oxide phases, which fill and seal microcracks, thereby preventing spallation and preserving surface integrity. The segregation is then constrained by the formation of Co_3O_4 when exposed to atmosphere, avoiding fully segregation and leaving a metastable core. This work demonstrates a pathway toward high-temperature coatings capable of self-repair, offering a strategy to improve the durability, reliability, and operational efficiency of next-generation gas turbine engines.

1 Introduction

Gas turbine engines are perfect examples of a demanding environment where scientists face many challenges in developing new materials. The surfaces are exposed to a gradient of temperatures, with temperature ranging from the ambient temperature up to 2000 °C [1]. One of the reasons for such extreme temperatures is the link between the turbine inlet temperature and the efficiency of such engines [2]. The interest in increasing these engine's efficiency is not retained to only economic aspects, but also environmental. An engine's efficiency is a key parameter to comply with the ambitious goal of the aviation sector of achieving net zero greenhouse gas emissions [3]. Other approaches, such as the use of sustainable aviation fuel (SAF) are also an option, replacing the regular kerosene-type fuels. One alternative SAF is hydrogen; however, the temperature challenge still persists, making the development of advanced materials essential [4]. Therefore, regardless of the approach used, the resistance of the surfaces to extreme temperatures is always linked to the efficiency that can be achieved in these engines.

Cobalt-based superalloys are often used in gas turbine engines due to their ability to stabilize a glaze layer that protects the surface from wear. Therefore, these alloys are widely used in tribological interfaces to control wear, such as blades [5,6] and seals [7,8] as shown in **Fig. 1 a-b**. In the specific case of the cobalt-based superalloy L605, this glaze layer is observed to be composed of cobalt and chromium oxides [9,10]. However, the wear resistance of such materials originates from the formation of the oxide layer and not the mechanical properties of these alloys. While more traditional nickel-based superalloys use precipitation hardening to improve the mechanical properties, this approach is more limited for cobalt-based alloys. Although developments in precipitation hardening are possible [11], the stability of such precipitates limits their application [12]. Moreover, the use of cobalt is usually minimized, due to costs associated with the raw materials that have been increasing due to demands for electrical vehicles [13]. On top of this further challenges such as higher density [14], caused by alloying elements such as tungsten, poorer mechanical properties [15], and supply risk [16] limit their use and create a demand for alternatives.

One of the first studies to show the effects of the oxidation during the sliding wear of metallic surfaces was Peterson et al. [17]. Later, F.H. Stott coined the term glaze layer to describe the formation of well-developed and homogeneous oxide films at metallic interfaces [18]. when metallic surfaces undergo tribo-oxidation at elevated temperatures, compact glaze layers can form from naturally occurring oxides [19]. If the layer is not well-compacted, however, loose hard particles may detach, leading to increased wear. Stott also introduced the concept of a critical temperature, below which the glaze does not stabilize, and wear rates increase. For a glaze layer to form, certain conditions must be met. One key mechanism is the "recycling process", wherein wear debris are sintered into protective surface layers [20]. This process is heavily influenced by the

tribological system and requires sufficient frictional heating or high ambient temperatures [19], as the glaze forms through tribo-sintering [21]. It was also observed that, depending on the interfacial surfaces, the glaze layer could form through mechanical mixing of material originating from both sides [22]. This process formation is summarized in **Fig. 1 c**.

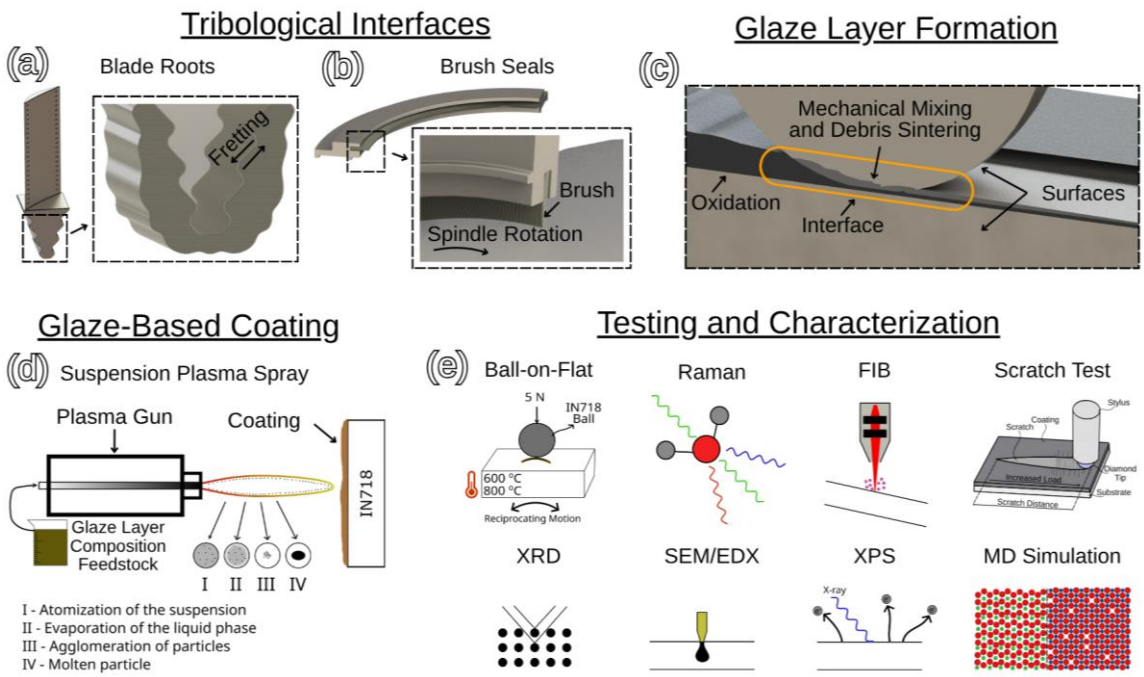

To mitigate the challenges with the glaze layer formation, coatings mimicking the chemical composition of such glaze layers were developed by suspensions plasma spray (SPS) using feedstock material with similar composition to the glaze layer developed by cobalt-based alloys, as shown in **Fig. 1 d**. It was observed that these coatings were highly wear resistant, and a potential candidate for improving the tribological properties of different alloys (e.g., Inconel 718). However, when characterizing such surfaces after tribological tests at 800 °C, segregation of cobalt was observed. This segregated material was observed to migrate to the free surfaces, creating a lubricious thin layer of CoO and Co_3O_4 at the top surface improving its tribological performance. Moreover, CoO migrated into cracks, further enhancing adhesion. This changed the focus of this study to understanding and taking advantage of such segregation as a healing mechanism. In addition to the tribology tests, a characterization of the interfaces using techniques such as sputtering x-ray photoelectron spectroscopy (XPS), high temperature x-ray diffraction (XRD), and Raman spectroscopy were further performed to understand the formation of this layer. Artificial defects were also introduced by performing scratches on the surface to assess the healing capabilities of the system. Insights into the formation of the segregate and self-healing mechanisms were developed based on the acquired experimental

data and supporting molecular dynamics simulations. The techniques for testing and characterization of the coatings and interfaces are summarized in **Fig. 1 e**.

2 Results and Discussion

2.1 Tribological Performance of the Glaze-Based Coatings

In this study, coatings were developed with different chemical compositions based on the glaze layer formed on cobalt-based superalloys [10] over Inconel 718 substrates by means of suspension plasma spray. As the composition of the glaze layer varies throughout the layer, two compositions (i.e., $CoO–21Cr_2O_3$ and $CoO–42Cr_2O_3$) were studied alongside a Cr_2O_3 coating for comparison. Their atomic composition measured by energy dispersive X-ray (EDX) is available in Supplementary Table 1. Dense coatings were developed, based on the parameters previously optimized [23], with the presence of micropores (**Fig. 2 a-c**). After spraying, mostly CoO and Cr_2O_3 were observed in X-ray diffractograms of the glaze-based coating (Supplementary Fig.1), with traces of $CoCr_2O_4$ for the $CoO–42Cr_2O_3$ coating. However, when analyzing polished cross sections by Raman spectroscopy more phases were revealed (Supplementary Fig. 2). Raman spectroscopy revealed the presence of $CoCr_2O_4$ for the $CoO–21Cr_2O_3$ coating and CrO_2 for the Cr_2O_3, phases, but these were not detectable by XRD, suggesting minor concentrations.

Tribology tests under two different temperatures were performed to simulate the environment observed in tribological interfaces within gas turbine engines. Inconel 718 counterfaces were used due to the wide application of such alloys in gas turbine engines. The results for the tests at 800 °C are shown in **Fig. 2 d-h**, and results obtained at 600 °C are similarly shown in Supplementary Fig. 3. Due to material transfer from the counterfaces, high concentrations of nickel, chromium and iron were observed at the wear tracks of all the tested specimens. Similar coefficients of friction were observed among the different coatings, as shown in **Fig. 2 g**. Raman spectroscopy analysis, **Fig. 2 h**, revealed peaks associated with spinel-like compounds. A minor exception was observed in the $CoO–21Cr_2O_3$ coating, where peaks corresponding to Co_3O_4 were detected, and indeed, less transferred material was observed on the wear track, **Fig. 2 d**. Recently spinel oxides originating from nickel-based superalloys were suggested to be key for their lubricity at elevated temperatures [24], likely contributing to the comparable friction behavior observed among these coatings.

Due to minimal material removal of the coatings, it was not possible to assess their wear behavior. Nonetheless, more substantial differences in wear were observed when analyzing the counterfaces (Supplementary Fig. 4). Even considered an abrasive oxide [25], lower wear was observed by counterfaces tested against the Cr_2O_3 coating at 600 °C. This performance can be attributed to the higher hardness of the

coating (Supplementary Table 2), which provides a hard surface that facilitates the shearing of the spinel-type oxide, producing an effect analogous to that of a thin soft coating over a hard substrate [26]. Such spinels were also observed in our previous study on cobalt- and nickel-based superalloys tested under similar conditions; however, the materials exhibited an order-of-magnitude higher total wear volume (i.e., counterface + surface) without a coating [22]. Nonetheless, although material removal was not observed after the tribology tests, cracks caused by different thermal expansion of the coating and substrate were observed. While for 600 °C cracks were observed at all conditions, Supplementary Fig. 3 a-c, at 800 °C the addition on CoO improved the resistance of the coating. For the Cr_2O_3 coating, only one tested specimen retained residual material that could be imaged, shown in **Fig. 2 f**. The other trials all resulted in complete spallation of the coating during the cooling after the tests, as shown in Supplementary Fig. 5. Although larger cracks were observed near the wear tracks, complete spallation of the coating occurred only after cooling. This suggests that the spallation originated from a combination of fatigue wear, followed by crack propagation driven by the mismatch in the coefficient of thermal expansion between the Cr_2O_3 coating and the substrate.

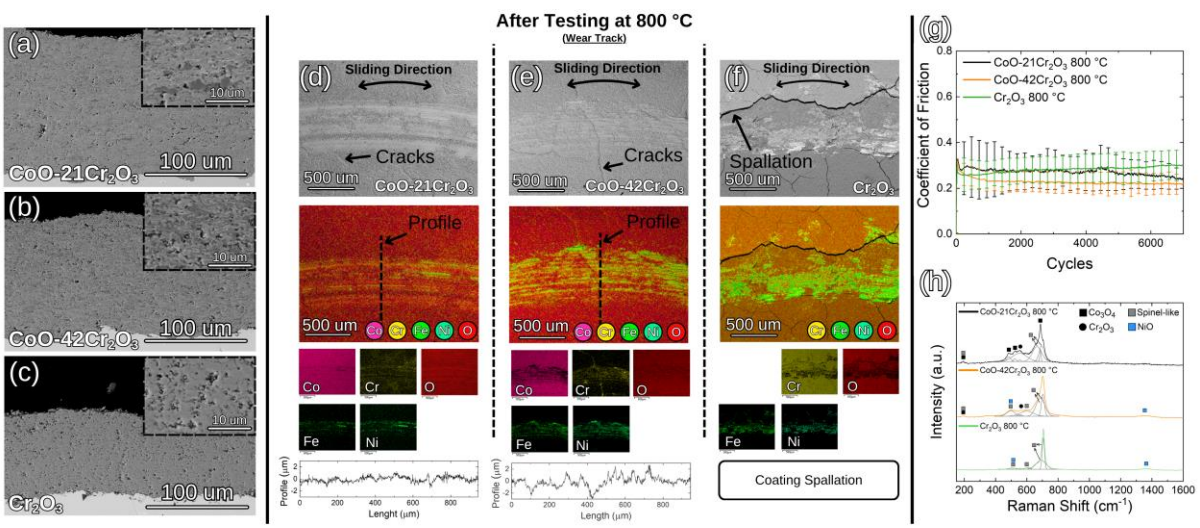

Improved performance was observed after adding CoO to the coating, **Fig. 2 d, e**, however, the sharpness of the cracks observed at 600 °C and 800 °C were different, with the 800 °C oddly appearing to perform better. Therefore, more detailed analyses were performed at the cross-section of these samples. FE-SEM micrographs from the cross section and XPS profiles of the samples are presented in **Fig. 3**. It was found that cobalt oxide could be observed as a segregated phase, segregating towards free surfaces. When analyzing outside of the wear track region, **Fig. 3 a-b**, different behaviour was observed for the CoO–21Cr_2O_3 and CoO–42Cr_2O_3 coatings. An angled view of these cracks further illustrates their propagation through the coating, as shown in Supplementary Fig. 6. It should be noted that in Supplementary Fig. 6 both surfaces were polished, so the top cobalt oxide layer was removed. The CoO–21Cr_2O_3 coating

developed a thicker surface layer of cobalt oxide, with certain regions corresponding to previously existing cracks. However, significantly fewer and less pronounced cracks were observed in this coating, **Fig. 2 d**, making it more difficult to clearly identify remnants of former crack paths. While one might argue that oxidation could lead to the formation of this surface layer, elemental mapping of the CoO–21Cr_2O_3 coating reveals a lower oxygen concentration in the segregated region, suggesting a different formation mechanism. Meanwhile, the CoO–42Cr_2O_3 presented a thinner top layer with more obvious features corresponding to previous cracks. The chemical composition of such layers measured by EDX is available in Supplementary Table 3.

Conventional metallographic techniques were unable to reveal significant differences between the cross-sections inside and outside the wear tracks. Consequently, FIB-milling was employed to investigate the cross-section, **Fig. 3 c-f**. For the outside of the wear track, the segregated layer was also observed in both conditions, **Fig. 3 c-d**, with a crystalline morphology showing visible grains. Interestingly, for the CoO–42Cr_2O_3 within the filled crack, **Fig. 3 d**, visible grains were not observed. The wear tracks, **Fig. 3 e-f**, showed differences among the samples. For the CoO–21Cr_2O_3 the formation of submicron grains was observed, caused by shearing of the surface. For CoO–42Cr_2O_3, larger grains were observed, representing mostly transferred material from the counterfaces. To gather more detail about these interfaces, X-ray photoelectron spectroscopy was performed at the wear track region of the coatings, **Fig. 3 g-h**. CoO–21Cr_2O_3, **Fig. 3 g**, correlating with the observed small transfer from the counterface, displayed traces of niobium and molybdenum in oxidized states without detectable presence of nickel. Cobalt and oxygen were the majority species observed, with minimal presence of chromium close to 1 at.%, correlating with the previous EDX analysis. For the case of CoO–42Cr_2O_3, **Fig. 3 h**, nickel was observed, suggesting a mechanical mixing with the counterface.

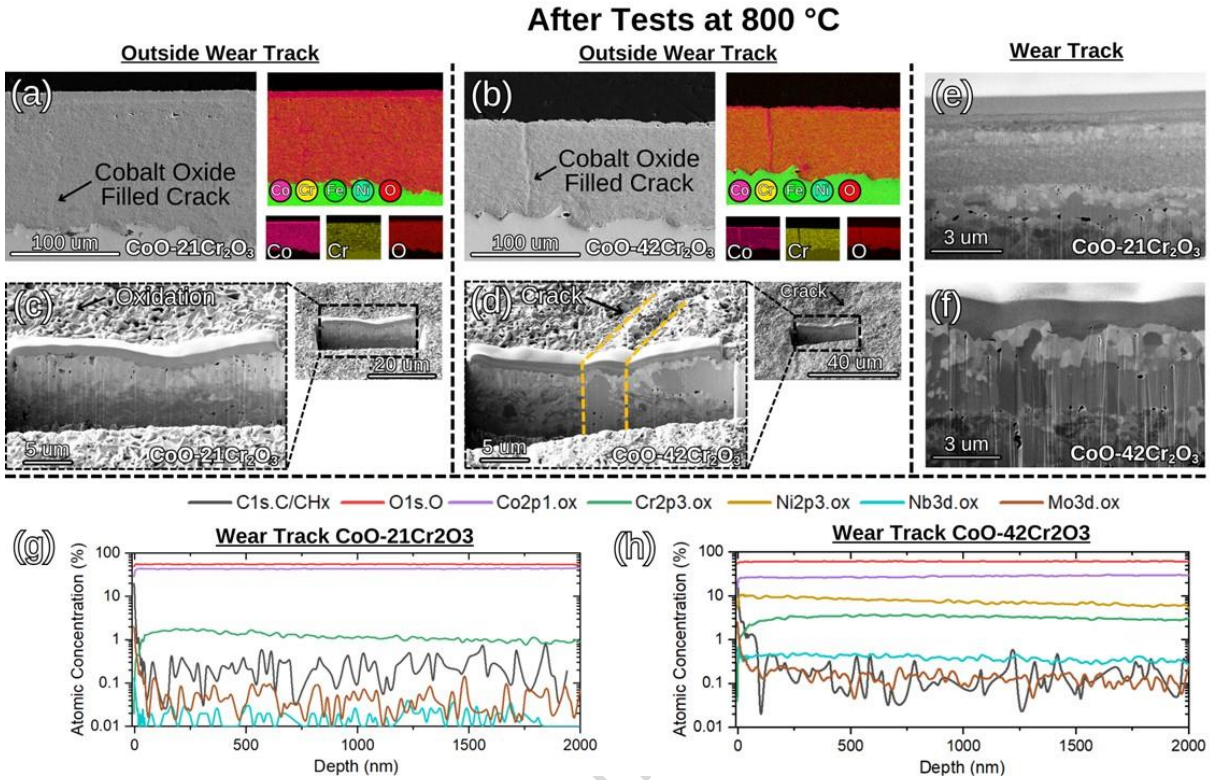

Due to the interesting formation of CoO/Co_3O_4 at the top surface, complemental tribological analysis of this layer was performed (Supplementary Fig. 7), as our previous study has shown that CoO offers excellent protection of the counterface at 600 °C [22]. This becomes even more compelling when considering that the formation of a soft microfilm over a hard coating can show improvements in friction and wear [26]. Therefore, a pre-oxidation of the surface under the same conditions as the tribological test was performed at 800 °C to create a segregated layer, with further tests under similar conditions performed at 600 °C. Despite no clear differences in the coefficients of friction, a slightly faster running-in period was observed. As expected, drastic reduction in the counterface wear was observed with no substantial wear of the coating.

2.2 Segregated Phase Composition

More in depth analyses were performed to gather information about the segregated material composition. Interestingly, a better contrast between CoO and Co_3O_4 is displayed when using optical microscopy, as observed in **Fig. 4 a**. Due to the inherent high spatial resolution of Raman spectroscopy, analyses were performed both on the top surface, **Fig. 4 b**, and cross section, **Fig. 4 (c, d)**. At the top surface (**Fig. 4 b**), the formation of sharp peaks related Co_3O_4 is observed. However, analysis of the segregated layer cross

section (**Fig. 4 c**) reveals a mixture of different stoichiometries, CoO and Co_3O_4. This correlates with the elemental mapping analysis (**Fig. 3 a**), where a lower concentration of oxygen is observed. The spectrum collected in the middle of the coating, (**Fig. 4 d**), shows the presence of mixed oxides, with an abnormal intensity of the peak at 197 cm^{-2}. Similar spectra were observed by other researchers for $CoCr_2O_4$ spinel-like compounds [27–29], showing a formation of $CoCr_2O_4$ from the CoO and Cr_2O_3 present originally in the coating. The thermodynamics of the CoO-Cr_2O_3 system were previously studied by Ostby and Chen, who found that at 800 °C (i.e., 1073 K) in low partial pressures of oxygen (i.e., inside the coating) two phases are thermodynamically stable, CoO and $CoCr_2O_4$ [30]. As there is a solubility limitation, the surplus segregates to the free surfaces through a chemical gradient, creating a layer at the top surface and filling cracks.

X-ray photoelectron spectroscopy (XPS) depth profiling revealed the composition within the top 2 µm of this layer, suggesting the oxidation of CoO → Co_3O_4. XPS analysis further revealed that the residual amount of oxidized chromium in this layer was minimal, with a peak concentration of only 0.4 at.%. Interestingly, the formation of Co_3O_4 is observed within the coating itself, occurring independently of atmospheric oxygen. This behavior is attributed to the non-stoichiometric and highly defective nature of the CoO crystal structure. Żyła et al. observed this phenomenon, attributing the formation to the decomposition of the CoO phase [31]. To have a better understanding of the phase segregation and its evolution, X-ray diffraction was performed at varying temperature (**Fig. 3 f**). At room temperature, the same phases as previously identified are present (i.e., CoO, Cr_2O_3, and $CoCr_2O_4$). At 600 °C the formation of Co_3O_4 is observed, either by atmospheric oxygen diffusion or CoO degradation. Similarly, the Co_3O_4 is present at 800 °C and remains when cooled back to room temperature.

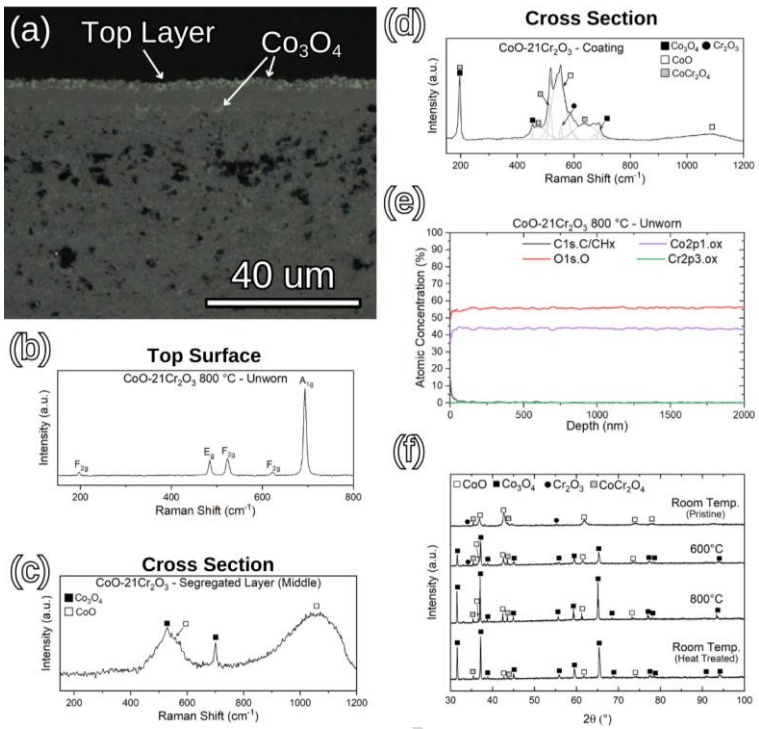

2.3 High-Temperature Self-Healing

The closing of cracks led to a hypothesis about the potential use of such coating as a self-healing system. To test it, artificial defects were introduced on the surface by instrumented scratch tests. **Fig. 5 a-c** shows the optical microscopy images of a scratch performed on the surface over time. The scratch on the pristine surface (i.e., polished and without prior thermal exposure) showed pronounced mechanical damage, with transverse cracks formed within the groove, accompanied by crack propagation beyond its boundaries and regions of interfacial delamination. After 2 hours of heating (**Fig. 5 b**), these mechanical defects mostly disappear, and after 8 hours (**Fig. 5 c**) they are barely visible. Although the scratch appears to disappear after 2 hours of testing (**Fig. 5 b**), analysis of the surface by confocal microscopy (**Fig. 5 d**) showed that remains of the scratch was still present. This effect is most likely a consequence of enhanced surface light scattering, originating from the roughness generated during oxidation. Nonetheless, with longer exposure times the maximum depth progressively decreased, and after 8 h at 800 °C the scratch was no longer discernible. One could argue that this effect was caused by the oxidation of the surface, and not by the phase segregation. However, similar tests were performed for a solely CoO coating, shown in Supplementary Fig. 8, where no healing is observed.

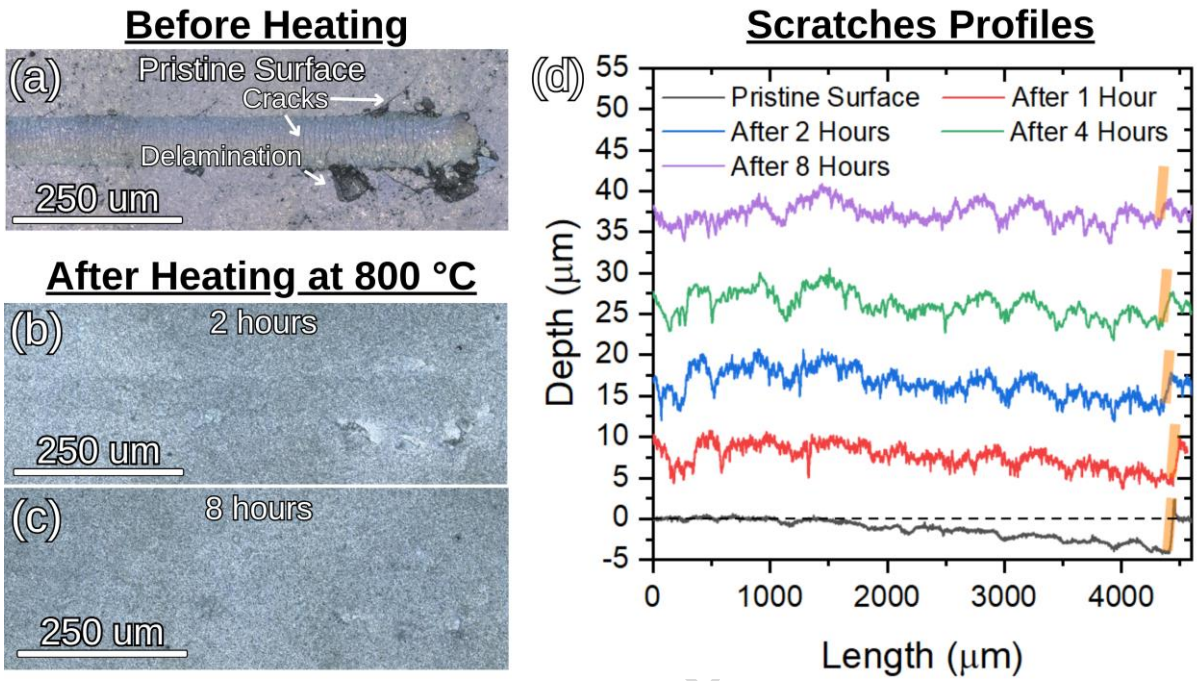

To observe the cross section of such defects, constant load scratches at 20 N were performed in different samples (**Fig. 6 a-d**). For the not heat-treated scratch (**Fig. 6 a**), only subsurface cracks are visible caused by the scratch. After 2 hours, (**Fig. 6 b**) subsurface cracks are no longe visible, and a segregated layer is observed at the free surface. After 4 hours (**Fig. 6 c**), the thickness of the segregated layer remains similar, but the oxidation to Co_3O_4 becomes more intense. The direction of growth of the Co_3O_4 (from top to bottom) indicates that this phase is formed mostly from diffusion of oxygen from the atmosphere, although internal oxidation is also observed, mostly close to pores. After 8 hours (**Fig. 6 d**) this layer was mostly transformed into Co_3O_4. The mapping at the same position (**Fig. 6 e**) shows the difference in oxygen concentration from the Co_3O_4 and CoO, having a cluster of CoO underneath the scratch region. Similar subsurface cracks, segregated layer evolution, and CoO cluster were observed in another set of tests performed with linear load scratches, as shown in Supplementary Fig. 9. For the sample tested for 8 hours it was possible to observe a crack outside of the scratch region, as shown in **Fig. 6 f**. The point analyses acquired by EDX from **Fig. 6 (e, f)** are shown in the Supplementary Fig. 10.

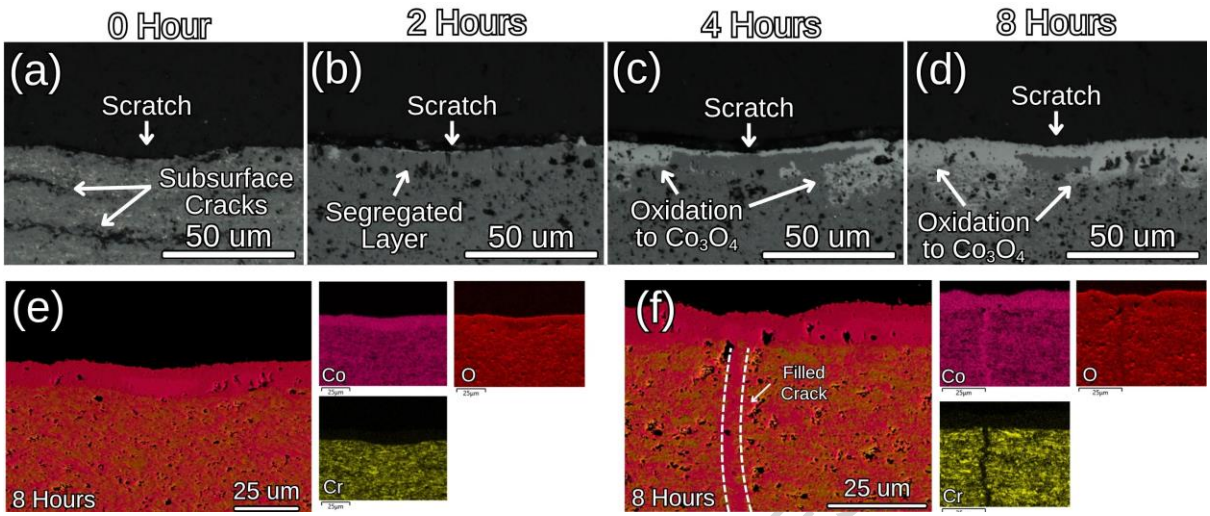

Fig. 7 summarizes the observations and illustrates the self-healing mechanisms of the glaze-based coatings. Two different healing mechanisms were observed. The primary mechanism and the one responsible for the coating integrity is shown in **Fig. 7 a**, having the system initially consisting of the coating and defects, such as cracks. Cobalt (II) oxide is known to have a rock salt-like crystal structure, as observed in the XRD analysis, **Fig. 4 e**, and to have a high concentration of cation vacancies, creating pathways for diffusion [32,33]. Chromium (III) oxide, however, has a corundum-like crystal structure, with low defect concentrations [34]. However, at high temperatures, the Cr_2O_3 reacts to form $CoCr_2O_4$, as observed in the CoO-Cr_2O_3 phase diagram at 800 °C [30]. Due to limited solubility, the surplus of CoO can segregate. Just small amounts of chromium were observed in this segregate, as the mobility of Cr^{3+} is several orders of magnitude lower than Co^{2+} in CoO [35]. While cobalt cations are transported preferably through the lattice, oxygen atoms diffuse more slowly as shown by the molecular dynamic simulations in **Fig. 7 b**. Therefore oxygen finds more preferable diffusion pathways through grain boundaries, as observed in other studies [36]. This leads to a highly mobile phase, required in self-healing materials [37]. When the CoO segregated layer is exposed to the environment, further oxidation into Co_3O_4 takes place. This formation of Co_3O_4 constrains further diffusion, as cobalt cations diffuse slower in Co_3O_4 [38,39] compared to CoO, slowing the segregation and causing the segregate layer to saturate at a thickness of around 8-10 µm in the conditions of this study for the CoO-21Cr_2O_3 coating. As this layer stops growing, diffusion of oxygen from the environment keeps oxidizing the CoO layer into Co_3O_4. Inside the filled cracks CoO was still found, as diffusion from the atmospheric oxygen did not reach the internal cracks. This creates a shell, leaving the surplus CoO inside the coating ready to segregate in the case of future cracks. A secondary healing mechanism was also

observed. When scratches on the surface were induced, as shown in **Fig. 7 b**, preferable segregation was observed in the region of the scratch, leading to healing of the scratch. Analysis of the cross-sections shows a cluster of CoO, and thinner layer of Co_3O_4 formed beneath the scratch. As the Co_3O_4 prevents further segregation of CoO, a delay in the formation of Co_3O_4 allows higher amounts of CoO to diffuse into the scratch groove, leading to healing.

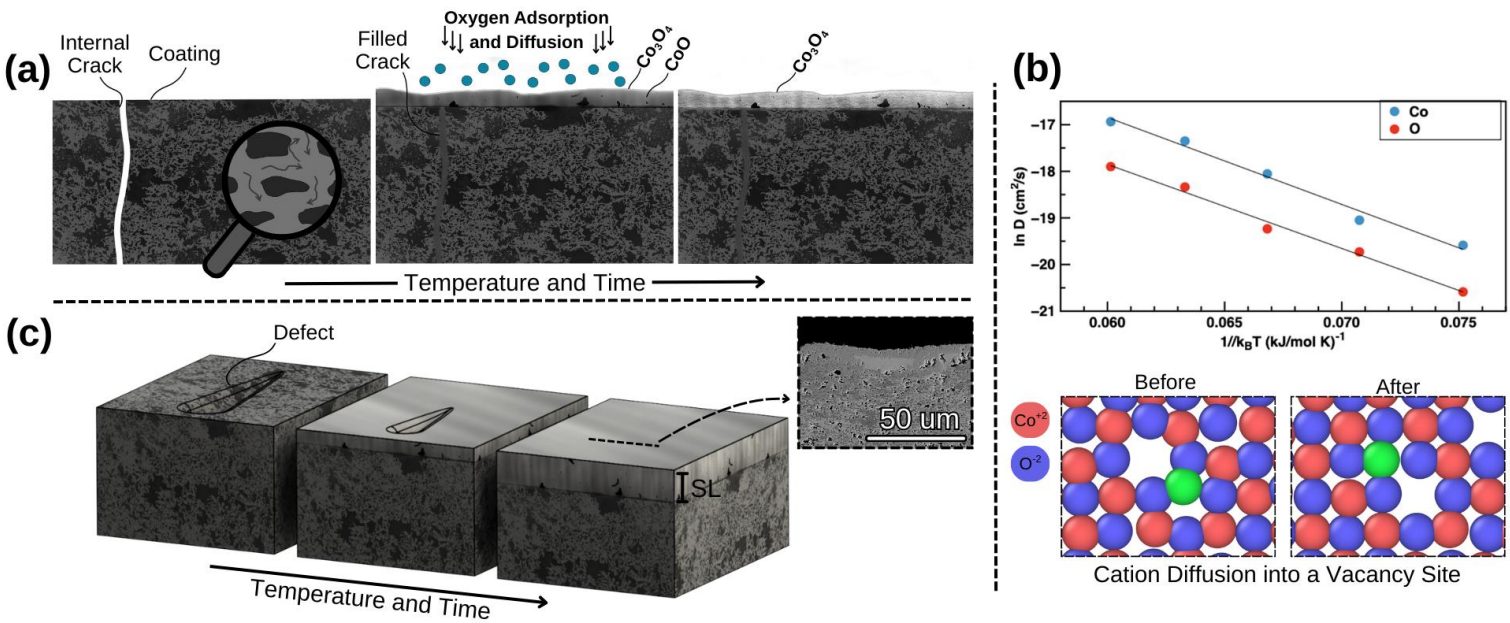

3 Conclusion

In summary, we demonstrate that phase segregation in the CoO–Cr_2O_3 system at elevated temperatures enables autonomous crack healing, allowing the material to self-repair damage induced by thermal stresses and significantly enhance surface durability. The CoO phase exhibits notable mobility, migrating toward free surfaces in a manner consistent with the morphology of natural glaze layers. The segregated phase not only improves surface integrity but also protects the counterface when pre-formed. These findings suggest that glaze-based coatings offer a promising alternative to cobalt-based superalloys, by mimicking the glaze-layer on more mechanically robust substrates such as nickel-based alloys. Furthermore, the use of engineered coatings eliminates the need for in-service glaze formation, bypassing requirements like debris retention and prolonged running-in periods, thus expanding their applicability to additional wear regimes, including sliding wear. By mimicking a glaze layer, multiple mechanisms were observed, bridging tribology, surface engineering, aerospace, and solid-state chemistry, underlining both the scientific depth and technological relevance of the development of surfaces and materials based on naturally formed glaze

layers. The understanding of these mechanisms should enable further development of self-healing ceramic coatings and related material systems based on similar design strategies. Future work could focus on improving process efficiency and reducing the time required to achieve effective healing.

4 Methods

4.1 Materials and Suspension Preparation

Cobalt (II) oxide (CoO, 99%, Pi-Kem, UK) and chromium (III) oxide (Cr_2O_3, 99%, Pi-Kem, UK) powders (d_{50} = 0.5 μm) were used as feedstock for the thermally sprayed coating. Nickel-based substrates (McMaster-Carr, USA) were cut to 25 × 25 × 7 mm and grit-blasted prior to coating. Suspensions (20 wt.% solids in ethanol, 99.9%) were prepared with polyvinylpyrrolidone (PVP, Sigma-Aldrich, Canada) at 1 wt.% relative to the solid load, dispersed by magnetic stirring and probe sonication (Q700, Qsonica, USA) for 15 min with intermittent pulses to limit heating.

4.2 Coating Deposition

Coatings were produced by suspension plasma spray (SPS) using an Axial III system (Mettech, Canada) under the conditions in Table 1. Gas composition values are given as volume percentages.

Table 1 | Suspension plasma spray deposition parameters for the coatings.

Parameter	Value	Unit
Plasma current	170	A
Power	74	kW
Total Gas Flow	220	L/min
Ar, N_2, H_2	80, 10, 10	%
Carrier gas (Ar) flow rate	15	L/min
Stand-off distance	75	mm
Traverse speed	1000	mm/s
Suspension feed rate	45	mL/min
Number of passes	30	-
Pre-heating passes	10	-

4.3 Microstructural, Mechanical, and Surface Characterization

Surface and microstructural analyses were performed using SEM (S-3400, Hitachi, Japan) and FE-SEM (SU8200, Hitachi, Japan), both equipped with energy dispersive X-ray spectroscopy (EDS) detector. Hardness was measured using a MVKH1 (Mitutoyo, Japan) Vickers microhardness tester with a load of

300g. X-ray diffraction (XRD) was conducted on a D8 Advance (Bruker, Germany) with Cu Kα radiation (λ = 1.54 Å) for room- and high-temperature scans. Raman spectra were acquired using an inVia system (Renishaw, UK) with a 532 nm laser and 50x objective. XPS was performed with a PHI 5000 VersaProbe II (Ulvac-PHI Inc., USA) using an Al Kα source focused on a 200 μm spot. FIB milling (Helios NanoLab DualBeam 650, Thermo Fisher Scientific, USA) produced 40 × 20 × 18 μm cross-sections, with imaging conducted at a tilt angle of 52°.

4.4 Tribological Testing

Tribological tests were performed on a POD 4.0 DUCOM tribometer (Ducom Instruments, USA) in ball-on-flat configuration using 10 mm Inconel 718 balls (RPG Balls, Italy) as counterfaces. Tests (n = 3 per condition) were run in angular oscillation mode at 1 Hz, with 10 mm track diameter and 30° reciprocating angle, under a 5 N normal load, at 600 °C and 800 °C in air. The parameters were chosen based on a previous study in which a glaze layer was successfully stabilized on a Haynes 25 alloy at 800 °C, thereby providing a basis for comparison. The surfaces were polished with 3 μm diamond suspension to a mirror finish and ultrasonically cleaned in distilled water prior to testing.

4.5 Molecular Dynamics Simulations

A simulation containing 510 atoms (18 A/side) was created from 64 unit cells of CoO in the rock salt structure with two atoms removed (one each of Co and O to preserve stoichiometry). All simulations were performed using the LAMMPS simulation code (Plimpton, S. Fast parallel algorithms for short-range molecular dynamics. *J Comput Phys* **117**, 1–19 (1995)[40]. Thompson, A. P. *et al.* LAMMPS-a flexible simulation tool for particle-based materials modeling at the atomic, meso, and continuum scales. *Comput Phys Commun* **271**, 108171 (2022)[41].) The structure was initially minimized to 0K followed by a 20 ps equilibration (timestep 1 fs) at a pressure of 1 atmosphere and temperatures ranging from 1600-2000K in an NPT simulation with a Nosé-Hoover thermostat and barostat. Following equilibration, mean squared displacement (MSD) data was taken separately for Co and O atoms over 10 ns, with data averaged over 10 blocks of 100 timesteps, dumped every 1000 timesteps. The MSDs were converted to diffusion using the Einstein relation (D=MSD/6) and fit with linear regression. The slopes of the lines were then used to calculate the diffusivity, as shown in **Fig. 7 b**.

4.6 Self-Healing Tests

Scratches were introduced using an MFT 5000 (Rtec, USA) with instrumented indentation/scratch module. Progressive-load scratches linearly ranged from 1–20 N over 4 mm distance; constant-load scratches were at 20 N over 2 mm distance, both conditions performed at 5 mm/min. Scratch evolution during high-temperature exposure was monitored by optical microscopy and surface profilometry using a Lext OLS4100 (Olympus, Japan). More details about the cross-section imaging of the scratches are provided in Supplementary Fig. 11.

For tracking the evolution of the scratch, the samples were introduced inside the furnace and timing started after the target temperature of 800 ℃ was reached. The heating cycles are shown in Supplementary Fig. 12. The samples were cyclically tested until reaching a cumulative time of 8 hours. For cross section analysis, to avoid cutting in different lengths of the scratch, a constant load scratch was performed over different samples exposed to the target temperature of 800 ℃ for 0, 2, 4, and 8 hours.

5 References

[1] M. R. Dorfman, G. Dwivedi, C. Dambra, S. Wilson, *J Therm Spray Tech* **2022**, *31*, 672.
[2] J. H. Perepezko, *Science* **2009**, *326*, 1068.
[3] L. L. Jensen, P. A. Bonnefoy, J. I. Hileman, J. T. Fitzgerald, *Progress in Aerospace Sciences* **2023**, *141*, 100921.
[4] E. Stefan, B. Talic, Y. Larring, A. Gruber, T. A. Peters, *International Materials Reviews* **2022**, *67*, 461.
[5] J. Feng, C. Qie, T. Chen, H. Liu, Y. Zhang, S. Zhang, L. Yuan, Y. Tian, *Lasers Manuf. Mater. Process.* **2025**, DOI 10.1007/s40516-025-00300-0.
[6] M. R. Barajas-Álvarez, A. Bedolla-Jacuinde, V. H. López-Morelos, A. Ruiz, *MRS Advances* **2022**, *7*, 1109.
[7] J. Derby, R. England, in *28th Joint Propulsion Conference and Exhibit*, American Institute Of Aeronautics And Astronautics, Nashville,TN,U.S.A., **1992**.
[8] T. Kirk, A. Bowsher, P. Crudgington, in *Volume 5B: Heat Transfer*, American Society Of Mechanical Engineers, Charlotte, North Carolina, USA, **2017**, p. V05BT15A003.
[9] A. Viat, G. Guillonneau, S. Fouvry, G. Kermouche, S. Sao Joao, J. Wehrs, J. Michler, J.-F. Henne, *Wear* **2017**, *392–393*, 60.
[10] A. Dreano, S. Fouvry, S. Sao-Joao, J. Galipaud, G. Guillonneau, *Wear* **2019**, *440–441*, 203101.
[11] J. Sato, T. Omori, K. Oikawa, I. Ohnuma, R. Kainuma, K. Ishida, *Science* **2006**, *312*, 90.
[12] A. Suzuki, H. Inui, T. M. Pollock, *Annu. Rev. Mater. Res.* **2015**, *45*, 345.
[13] R. T. Nguyen, R. G. Eggert, M. H. Severson, C. G. Anderson, *Resources, Conservation and Recycling* **2021**, *167*, 105198.
[14] K. Luo, S. Li, G. Xu, S. R. E. Hosseini, J. Lu, *Corrosion Science* **2022**, *197*, 110040.
[15] B. Nithin, A. Samanta, S. K. Makineni, T. Alam, P. Pandey, A. K. Singh, R. Banerjee, K. Chattopadhyay, *J Mater Sci* **2017**, *52*, 11036.
[16] A. L. Gulley, *Resources Policy* **2022**, *79*, 103007.
[17] M. B. Peterson, J. J. Florek, R. E. Lee, *A S L E Transactions* **1960**, *3*, 101.
[18] F. H. Stott, D. S. Lin, G. C. Wood, *Nature Physical Science* **1973**, *242*, 75.
[19] F. H. Stott, *Tribology International* **1998**, *31*, 61.
[20] J. Jiang, F. H. Stott, M. M. Stack, **n.d.**
[21] A. Dreano, S. Fouvry, G. Guillonneau, *Wear* **2019**, *426–427*, 712.
[22] A. R. Mayer, O. Zouina, M. Dienwiebel, C. Moreau, P. P. Stoyanov, *Wear* **2025**, 205972.
[23] A. R. Mayer, B. C. N. M. De Castilho, A. Roy, F. B. Ettouil, C. Moreau, P. P. Stoyanov, *Surface and Coatings Technology* **2025**, *513*, 132545.
[24] Z. Zhang, E. Hershkovitz, Q. An, L. Liu, X. Wang, Z. Deng, G. Baucom, W. Wang, J. Zhao, Z. Xin, L. Moore, Y. Yao, M. R. U. Islam, X. Chen, B. Cui, L. Li, H. Xin, L. Li, H. Kim, W. Cai, *Nat Commun* **2024**, *15*, 10039.
[25] M. B. Peterson, J. J. Florek, R. E. Lee, *A S L E Transactions* **1960**, *3*, 101.
[26] K. Holmberg, H. Ronkainen, A. Matthews, *Ceramics International* **2000**, *26*, 787.
[27] M. Mączka, M. Ptak, M. Kurnatowska, J. Hanuza, *Materials Chemistry and Physics* **2013**, *138*, 682.
[28] N. Noor, A. Bagri, S. Sarkar, K. Dey, B. Krishna De, V. Sathe, R. J. Choudhary, A. Mishra, *Journal of Magnetism and Magnetic Materials* **2024**, *600*, 172131.
[29] V. Jagadeesha Angadi, K. Manjunatha, M.-K. Ho, S. Y. Wu, M. Ubaidullah, A. M. Al-Enizi, B. Pandit, B. Chethan, *J Inorg Organomet Polym* **2024**, *34*, 1712.
[30] J. Östby, M. Chen, *Journal of Alloys and Compounds* **2009**, *485*, 427.
[31] M. Żyła, G. Smoła, A. Knapik, J. Rysz, M. Sitarz, Z. Grzesik, *Corrosion Science* **2016**, *112*, 536.
[32] J. A. Van Orman, K. L. Crispin, *Reviews in Mineralogy and Geochemistry* **2010**, *72*, 757.
[33] P. S. Maiya, W. K. Chen, N. L. Peterson, *Metall Trans* **1970**, *1*, 801.
[34] A. Atkinson, in *Studies in Inorganic Chemistry*, Elsevier, **1989**, pp. 29–54.

[35] K. KOWALSKI, E.-G. Moya, J. Nowotny, **n.d.**
[36] U. Chowdhry, R. L. Coble, *J American Ceramic Society* **1982**, *65*, 336.
[37] S. M. Aouadi, J. Gu, D. Berman, *Journal of Vacuum Science & Technology A: Vacuum, Surfaces, and Films* **2020**, *38*, 050802.
[38] A. Kaczmarska, Z. Grzesik, S. Mrowec, *High Temperature Materials and Processes* **2012**, *31*, 371.
[39] K. Przybylski, W. W. Smeltzer, *J. Electrochem. Soc.* **1981**, *128*, 897.
[40] S. Plimpton, *Journal of Computational Physics* **1995**, *117*, 1.
[41] A. P. Thompson, H. M. Aktulga, R. Berger, D. S. Bolintineanu, W. M. Brown, P. S. Crozier, P. J. In 'T Veld, A. Kohlmeyer, S. G. Moore, T. D. Nguyen, R. Shan, M. J. Stevens, J. Tranchida, C. Trott, S. J. Plimpton, *Computer Physics Communications* **2022**, *271*, 108171.

Figure Captions

Fig. 1 | Glaze Layer Formation at Tribological Interfaces and Associated Replication and Characterization Methods. a-b Examples of tribological interfaces. **c** Formation mechanisms of the glaze layers. **d** Schematic of the thermal spray process used for the development of the glaze-based coatings. **e** Testing and characterization techniques used for analyzing the coatings.

Fig. 2 | Tribological Performance of the Developed Coatings at 800 °C. a-c Backscattered-electron SEM micrographs from the cross section of the studied coatings. Insets show higher magnification micrographs. The glaze-based coatings are the mixed composition **(a, b)** while a purely chromium (III) oxide coating is shown for comparison in **c**. **d-f** Backscattered-electron FE-SEM micrographs, energy dispersive X-ray (EDX) elemental mapping, and linear profile of the wear tracks observed on the developed coatings (CoO-21Cr_2O_3, CoO-42Cr_2O_3, Cr_2O_3) after testing against Inconel 718 counterfaces at 800 °C. **g** In-situ measurement of the coefficient of friction from the ball-on-flat tests. Error bars show the standard deviation from three tests. **h** Ex-situ Raman spectra from the compounds observed at the coating surface after tribological tests.

Fig. 3 | Cross-Section of the Glaze-Based Coatings After Tribology Tests at 800 °C. a-b Secondary-electron FE-SEM micrographs of the coatings at the outside of the wear track alongside their respective EDX elemental mapping analyses. **c-f** Secondary electron SEM micrographs from focused ion beam cuts. **(c, d)** depicts the effect of heating only while **(e, f)** presents the regions at the inside of the wear tracks. **(g, h)** X-ray photoelectron spectroscopy (XPS) depth profiles after sputtering at the wear track region. A logarithmic y-axis was employed to display elements with minor concentrations.

Fig. 4 | Composition of the Segregated Phase Observed in the CoO–21Cr_2O_3 Coating. a Optical Microscopy (OM) of the segregated layer observed in the CoO–21Cr_2O_3 after tribological tests at 800 °C. **b-d** Raman Spectra of the top surface **(b)** and cross sections of the segregated layer **(c)** and in the middle of the coating **(d)**. **e** X-ray photoelectron spectroscopy (XPS) depth profiles after sputtering. **f** X-ray diffraction performed at different temperatures. Pristine indicates the polished surface using a 3 µm diamond suspension. Heat treated indicates the surface after cooling back to room temperature from the previously analysis.

Fig. 5 | CoO–21Cr_2O_3 Coating Healing from Artificially Induced Defects on the Top Surface. a Optical microscopy (OM) image of a linear load scratch performed over the polished surface from 1-20 N at velocity 5 mm/min using a 200 µm diameter diamond Rockwell tip. **b, c** The OM image of the scratch after heat treatment at 800 °C for 2 **(b)** and 8 **(c)** hours. **d** Axially measured profiles from the scratch at different heat treatment periods. Yellow bars indicate the maximum depth at the end of the scratch. All heat treatments were performed with the furnace operating in atmospheric air.

Fig. 6 | CoO–21Cr_2O_3 Coating Healing from Artificially Induced Defects in the Cross-Section. a-d Cross sections of constant load scratches performed using same tip and velocities at 20 N load after different heat treatment periods at 800 °C. **e** Depicts the EDX mapping from the same position as **(d)**. **f** Depicts a region filled by cobalt oxide in a different region. All heat treatments were performed with the furnace operating in atmospheric air.

Fig. 7 | High-temperature healing model for glaze-based coatings. a Schematic of the cross-section defects following phase segregation, enabling defect healing. **b** Diffusion coefficient versus inverse thermal energy obtained

by molecular dynamics simulation. Insets from the simulation shows the moments just before and after the diffusion of the Co^{2+} cation **c** Segregation towards surface covering a top defect. SL stands for segregated layer.

Acknowledgements

The authors gratefully acknowledge the financial support provided by the Natural Sciences and Engineering Research Council of Canada (NSERC) through the Alliance Grants program (ALLRP 571542 - 21) and by the Fonds de recherche du Quebec – Nature et technologies (FRQNT) under the NOVA program.

Sandia National Laboratories is a multi mission laboratory managed and operated by National Technology &Engineering Solutions of Sandia, LLC, a wholly owned subsidiary of Honeywell International Inc., for the U.S. Department of Energy's National Nuclear Security Administration under contract DE-NA0003525. This paper describes objective technical results and analysis. Any subjective views or opinions that might be expressed in the paper do not necessarily represent the views of the U.S. Department of Energy or the United States Government.

Author Contributions

A.R. Mayer and P.P. Stoyanov conceived the present study. A.R. Mayer designed the experiments. O. Zouina performed the FIB and XPS analyses. M. Chandross performed the molecular dynamics simulations. M. Dienwiebel provided testing facilities, and C. Moreau provided coating facilities. P.P. Stoyanov, C. Moreau, and M. Dienwiebel provided supervision. A.R. Mayer wrote the first draft of the manuscript. P.P. Stoyanov acquired funding. All authors discussed the results and reviewed the manuscript.

Competing Interests

The authors declare no competing interests.

Data Availability

The data that support the findings of this study are available from the corresponding author upon reasonable request.

Editorial summary:

Gas turbine engines operate under extreme thermal and mechanical stresses, where material degradation through crack formation and surface wear can occur. This paper reports a self-healing coating based on phase segregation in the $CoO–Cr_2O_3$ system that repairs thermally induced cracks at elevated temperatures.

Peer review information:

Communications Materials thanks Wataru Nakao and the other, anonymous, reviewer(s) for their contribution to the peer review of this work. A peer review file is available.